JACS
JOURNAL OF THE AMERICAN CHEMICAL SOCIETY
pubs.acs.org/JACS
Article

In Situ SERS Monitoring of Plasmon-Mediated Degradation of Microplastics

Junyeong Yang, Minchu Kang, Ramesh Kumar Chitumalla, Emiliano Cortés, Joonkyung Jang, and Seunghoon Lee*

Cite This: J. Am. Chem. Soc. 2026, 148, 3462−3471
Read Online
ACCESS | Metrics & More | Article Recommendations | Supporting Information

ABSTRACT: Microplastics (MPs) are chemically stable and environmentally persistent pollutants that accumulate in natural ecosystems, posing potential risks to both environmental and human health. Despite growing concern, effective strategies for degrading MPs and elucidating their chemical transformations remain limited. In this study, we demonstrate plasmon-mediated degradation of polyethylene (PE) microplastics in aqueous solution using Au nanoparticle clusters (NPCs) under visible light irradiation. Nanogaps within the Au NPCs act as plasmonic hot spots, where hot carriers are generated and utilized in the degradation process, while the enhanced electromagnetic fields enable surface-sensitive detection of chemical changes via surface-enhanced Raman scattering (SERS). By leveraging the integrated catalytic and spectroscopic capabilities of Au NPCs, we conducted real-time SERS monitoring to reveal the plasmon-mediated degradation mechanism of PE MPs.

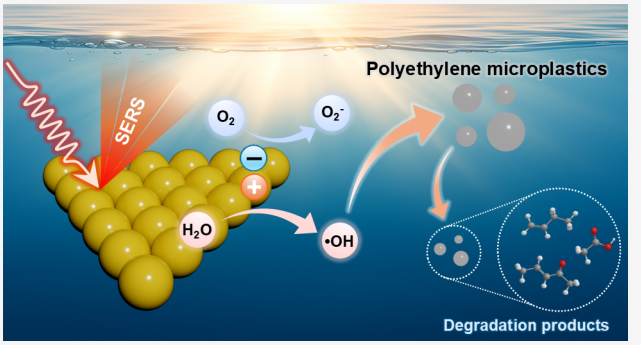

INTRODUCTION

Plastics are essential components of modern society owing to their durability, affordability, and versatility. However, these same properties have led to the global accumulation of persistent plastic waste. It is estimated that more than 80% of discarded plastics are released into the environment without proper management.[1,2] Over time, larger debris fragments into microplastics (MPs), particles with a diameter of less than 5 mm, which are ubiquitously detected in aquatic, terrestrial, and even atmospheric environments.[3−7] Their small size and large volume-to-surface area, combined with inherent resistance to degradation, enable long-term persistence and facilitate the adsorption of hazardous compounds. These features amplify ecological and human health risks.[8−10]

To address these risks, numerous degradation strategies have been investigated, including thermal, biological, and photocatalytic approaches. Thermal methods require high energy input and often produce undesirable byproducts,[11−14] while environmental conditions and substrate specificity constrain biological methods.[15,16] Photocatalysis has attracted tremendous interest as a more sustainable alternative because it utilizes light energy to activate degradation under mild conditions.[17−29] Most reported photocatalytic systems rely on semiconductors, but these typically require UV irradiation due to their wide band gaps, which limits their efficiency under solar-relevant visible light.[17−23] To overcome these drawbacks, visible-light active photocatalysts have been developed and applied to plastic degradation.[24−29] Despite this progress, extended irradiation times and limited mechanistic insight—particularly at plastic interfaces—remain persistent challenges.[20−23,26,29]

Plasmonic nanostructures offer an alternative route for efficient chemical energy conversion by harvesting visible light through localized surface plasmon resonances (LSPRs).[30−32] The decay of LSPRs generates energetic hot carriers—hot electrons and hot holes—that can drive diverse chemical reactions under mild conditions.[31−39] A key design principle to enhance plasmonic performance is the assembly of nanoparticles into architectures containing nanogaps. These junctions create intense electromagnetic fields, so-called "hot spots", that both amplify hot carrier generation for catalysis and enhance molecular detection sensitivity.[36−41] This dual capability is particularly relevant for plasmonic catalysis, where molecular-level characterization is essential. Conventional vibrational spectroscopy, such as Fourier transform infrared (FTIR) and Raman, has provided valuable information on polymer degradation, but both face limitations in resolution,

Received: October 26, 2025
Revised: December 30, 2025
Accepted: December 31, 2025
Published: January 6, 2026

https://doi.org/10.1021/jacs.5c18907
J. Am. Chem. Soc. 2026, 148, 3462−3471

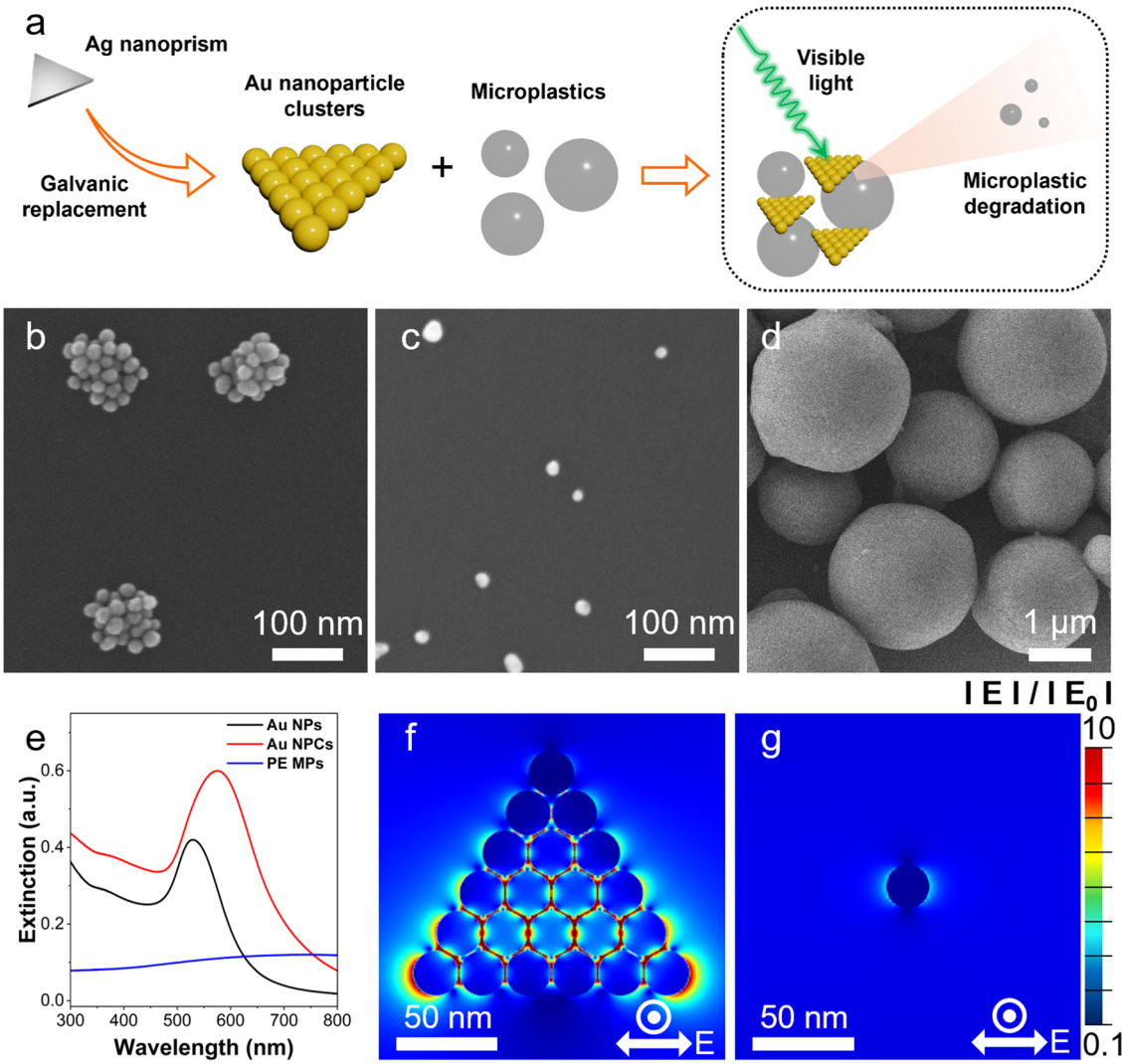

Figure 1. Characterization of Au NPCs, NPs, and PE MPs. (a) Schematic of photocatalytic degradation of PE MPs. SEM images of (b) Au NPCs, (c) Au NPs, and (d) PE MPs. (e) UV−vis spectra of Au NPCs (red), Au NPs (black), and PE MPs (blue) in colloidal solutions. FDTD simulated $|E|/|E_0|$ distributions of (f) Au NPCs and (g) Au NPs under broadband excitation from 400 to 800 nm, corresponding to the spectral range of the visible LED lamp used in the photocatalytic degradation of PE MPs.

sensitivity, and surface selectivity.[10,42,43] In this context, surface-enhanced Raman scattering (SERS), where plasmonic substrates amplify Raman and provide surface-specific molecular information, has emerged as a powerful complement.[43−48]

Here, we employ Au nanoparticle clusters (NPCs) with densely packed nanogaps as both plasmonic catalysts and SERS platforms to study plastic degradation. We demonstrate for the first time that Au NPCs effectively drive the plasmon-mediated degradation of polyethylene microplastics (PE MPs) under visible-light irradiation, whereas isolated Au NPs under the same conditions show negligible degradation. This contrast highlights the pivotal role of nanogap hot spots in enabling plasmon-mediated reactions. Through reactive-species control experiments, we further identify hot hole-mediated hydroxyl radicals as the dominant species responsible for PE MP degradation. Finally, we monitored the plasmon-mediated degradation of PE MPs via in situ SERS tracking, which provides surface-selective, real-time insight into molecular transformations in aqueous environments. This combined catalytic and spectroscopic platform not only confirms hydroxyl radicals as key intermediates but also introduces a new vibrational marker at 2924 cm^{-1} associated with diverse degradation products, thereby advancing mechanistic understanding of plasmon-mediated plastic degradation and highlighting opportunities for plasmon-enabled environmental remediation.

RESULTS AND DISCUSSION

Synthesis of Plasmonic Catalysts for PE MP Degradation

To enable plasmon-mediated degradation of PE MPs under visible light, we synthesized Au NPCs via a galvanic replacement reaction using silver nanoprisms as sacrificial templates, following our previously reported procedure.[41,44] As shown in Figure 1a, the Ag nanoprisms guided the formation of colloidal Au NPCs, comprising densely packed assemblies of tens of Au NPs, while retaining the overall morphology of the original template. The resulting Au NPCs were mixed with PE MPs in aqueous media and exposed to a broadband visible light LED irradiation, which covers the wavelength from 400 to 800 nm. The Au NPCs with average cluster, gap, and particle

https://doi.org/10.1021/jacs.5c18907
J. Am. Chem. Soc. 2026, 148, 3462−3471

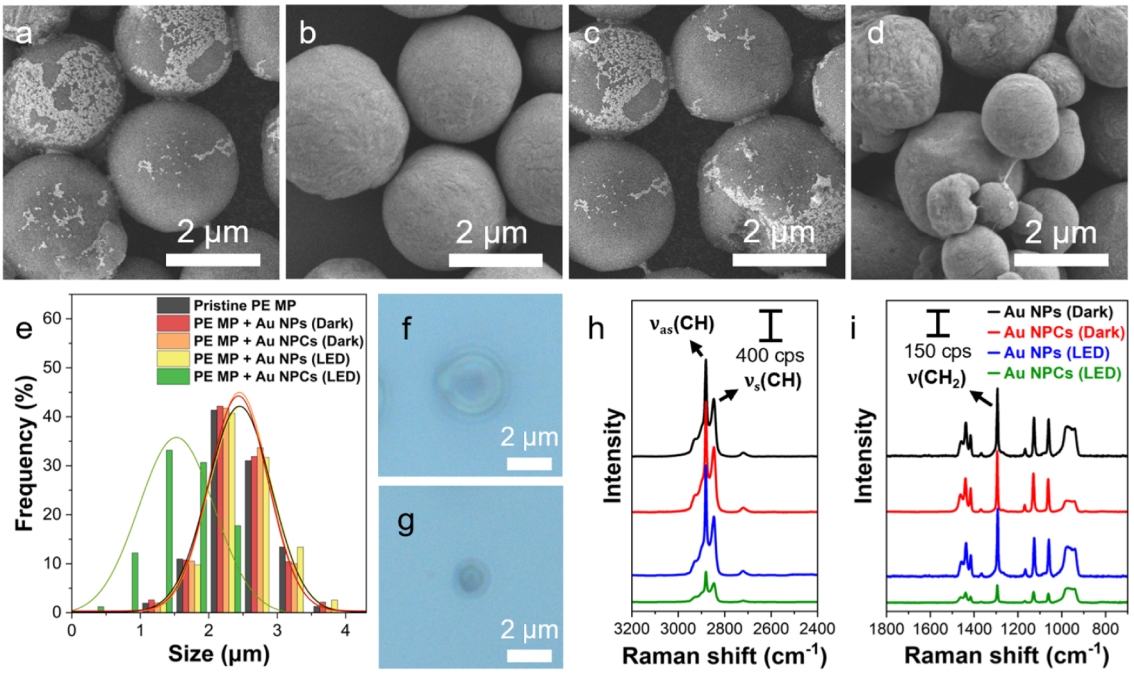

Figure 2. Comparative plasmonic degradation of PE MPs using Au NPs and NPCs. SEM images of the PE MPs treated for 12 h with (a) Au NPs and (b) Au NPCs in the dark, and with (c) Au NPs and (d) Au NPCs under LED illumination. (e) The size distribution of PE MPs before and after 12 h of treatment under each condition shown in (a–d). (f, g) Optical microscopy images of a single PE MP used for Raman measurements. The PE MP particles were sampled (f) before and (g) after 12 h of LED illumination under Au NPC reaction conditions, followed by removal of Au NPCs before imaging and Raman analysis. (h, i) Raman spectra of PE MPs collected after reaction, measured using a 532 nm excitation laser and averaged over 20 measurements from different positions on a single MP particle (*h*: 3200–2400 cm^{-1} *i*: 1800–700 cm^{-1}).

sizes of 118 ± 8, 0.6 ± 0.1, and 22 ± 2 nm, respectively, featured numerous subnanometer interparticle gaps that can act as plasmonic hot spots (Figure 1b and Figure S1). Each cluster comprises an average of 31 ± 3 individual AuNPs, forming multiple interparticle junctions where the electromagnetic field is strongly confined (Figure S2). To serve as a control, the Au NPs of comparable particle size (22 ± 5 nm) were synthesized (Figure 1c and Figure S3). The PE MPs, used as target substrates for degradation, were prepared as spherical particles with an average particle size of 2.5 ± 0.5 μm. (Figure 1d and Figure S4). UV–vis extinction spectra showed distinct optical responses for Au NPs and Au NPCs dispersed in aqueous solution (Figure 1e). Notably, Au NPCs exhibited significantly stronger and spectrally broader extinction across the visible range compared to Au NPs, which can be ascribed to interparticle plasmonic coupling within the assembled nanostructures.[41] Given that the particle concentration of Au NPs and Au NPCs—where the concentration for NPCs refers to the number of constituent particles within the clusters—was set to be a similar value, 1.56×10^{11} NPs/cm^3, matching those used in the PE MP degradation experiments, a direct comparison of their plasmonic and catalytic performance could be ensured. In contrast, PE MPs showed negligible extinction in the visible region (Figure 1e). Figure 1f,g show the FDTD-simulated EM field amplitude (|E|) distributions for an Au NPC and NP, respectively, under broadband excitation from 400 to 800 nm. The NPC exhibited pronounced near-field enhancement localized at the subnanometer interparticle gaps, with the maximum |E| reaching up to 30 times that of the isolated NP counterpart. The strong optical extinction and E-field confinement of Au NPCs in the visible range may contribute to hot carrier generation, highlighting their potential as promising plasmonic catalysts for light-to-chemical energy conversion.

Plasmon-Mediated Degradation of PE MPs

To establish a proof-of-concept for plasmon-driven degradation of PE MPs, we employed Au NPCs as plasmonic catalysts based on their enhanced plasmonic performances under visible light irradiation. The photocatalytic setup consisted of aqueous dispersions of PE MPs and plasmonic catalysts illuminated by a broadband visible LED source (400–800 nm, 410 mW/cm^2) (Figure S5, see the details for experimental conditions in SI). The reactions were performed for 12 h in the presence of either Au NPs or NPCs under dark and illuminated conditions. Figure 2a–d shows SEM images of the resulting PE MPs obtained under each condition. Under dark conditions, both Au NPs and Au NPCs resulted in negligible changes in MP size and morphology (Figure 2a,b), indicating the absence of significant degradation. In contrast, illumination with the visible LED lamp in the presence of Au NPCs induced pronounced morphological changes, including notable size reduction (Figure 2d), while Au NPs under identical conditions led to negligible changes in the size of MPs (Figure 2c). The average MP diameter decreased from 2.5 to 1.66 μm after reaction with Au NPCs under light irradiation (Figure 2e).

To further characterize the reacted MPs, we measured Raman spectra of MPs at the single particle level after 12 h of reaction using 532 nm excitation, which is one of the promising tools for identifying micro- and nano plastics.

Figure 2f,g shows representative optical microscopy images of a single PE MP collected before and after reaction with the Au NPCs under LED irradiation, followed by removal of residual catalysts. These images illustrate the typical procedure

https://doi.org/10.1021/jacs.5c18907
J. Am. Chem. Soc. 2026, 148, 3462–3471

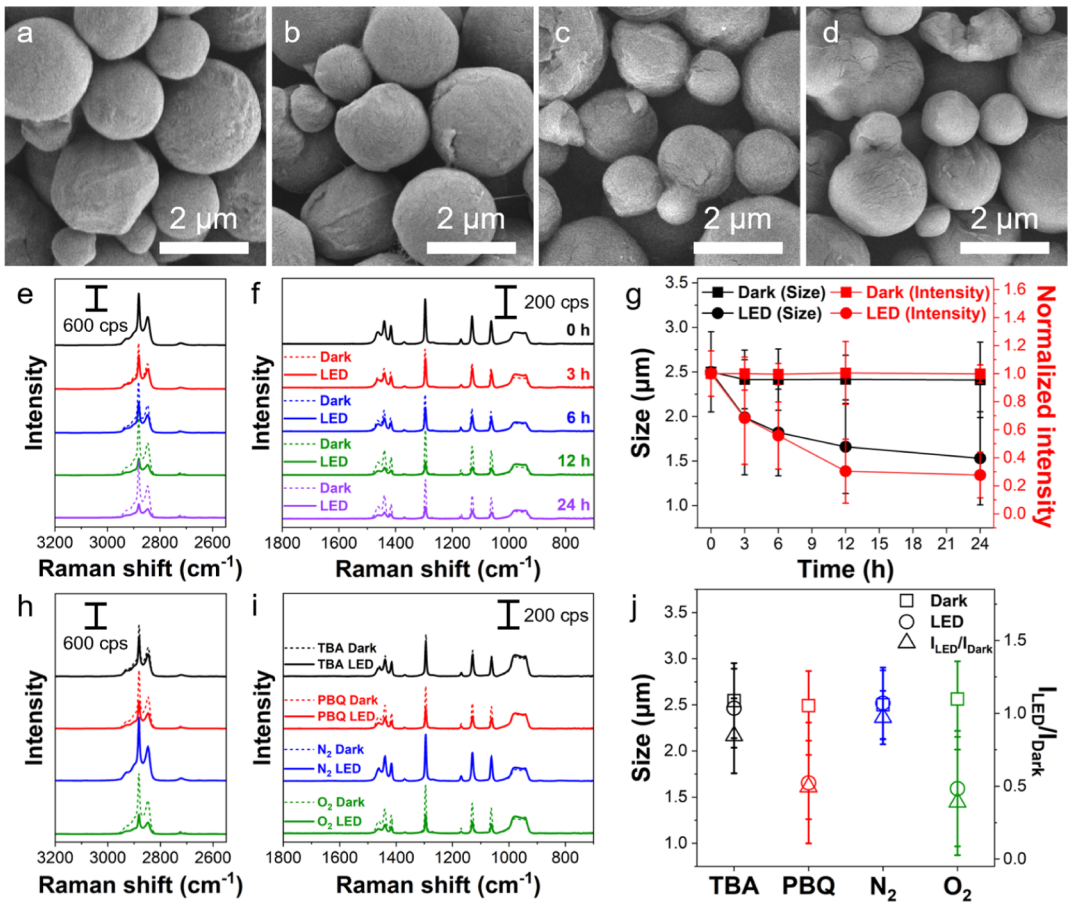

Figure 3. Plasmon-mediated degradation of PE MPs by Au NPCs under varied reaction conditions. SEM images of PE MPs collected after (a) 3, (b) 6, (c) 12, and (d) 24 h of visible LED illumination in the presence of Au NPCs. (e, f) The Raman spectra of MPs were collected at different reaction times (0, 3, 6, 12, and 24 h) after reactions under either dark (dashed lines) or LED-illuminated (solid lines) conditions. (g) The time-dependent changes in the average MP size (black, left axis) and the normalized Raman intensity of the $-CH_2$ twisting mode at 1294 cm^{-1} (red, right axis) under dark and LED conditions. (h, i) Raman spectra of MPs collected after 3 h of reaction under various conditions—TBA (black), PBQ (red), N_2-saturated (blue), and O_2-saturated (green) environments—each conducted under dark (dashed lines) and LED-illuminated (solid lines) conditions. (j) The plots of the reacted MP size and the Raman intensity ratio (I_{LED}/I_{Dark}) of 1294 cm^{-1} for each condition shown in (i). Each Raman spectrum was obtained using a 532 nm excitation laser and represents the average of 20 measurements acquired from different positions on a single MP particle.

used to identify individual MPs for Raman analysis; the same imaging and sampling protocol was consistently applied across all experimental conditions to ensure comparability in data acquisition. Raman spectra were averaged over 20 different positions for each particle in both the C−H stretching region (2800−3000 cm^{-1}, Figure 2h) and the vibration region corresponding to C−C stretching and CH_2 bending modes (700−1500 cm^{-1}, Figure 2i).[49]

PE MPs treated with Au NPCs under LED illumination exhibited a significant decrease in Raman intensity in both spectral regions compared to other experimental conditions, consistent with the size reduction observed in SEM (Figure 2e). The concurrent decrease in particle size and Raman signal intensity together indicates progressive degradation of PE. To further examine the possible contribution of particle size to Raman attenuation, we measured the signal from PE MPs with diameters ranging from 1 to 4 μm under identical excitation conditions (Figure S6). The attenuation of Raman intensity correlated well with the observed reduction in MP size, consistent with previously reported size-dependent Raman scattering intensity in polymer particles.[50]

While Raman spectroscopy enabled spatially resolved chemical characterization at the single particle level, complementary IR analysis faced intrinsic sensitivity limitations. When IR samples were prepared using the same protocol as for Raman measurements, the reacted MPs yielded no discernible spectral features owing to the extreme dilution of degradation products. To overcome this, the products were concentrated by solvent evaporation and subsequently redispersed in a minimal volume of cyclohexane before IR measurement (see Supporting Information for details, Figure S7). To exclude the direct photolysis, PE MPs were exposed to the same visible LED illumination without plasmonic catalysts. After 12 h, SEM images and Raman spectra showed no significant changes in size or spectra features (Figure S8), confirming that visible light alone does not induce degradation. Notably, the Au NPCs retained their morphology and photocatalytic activity over repeated reaction cycles (Figure S9 and S10), supporting their robustness and recyclability under the illumination conditions. Collectively, these results indicate that the Au NPCs enable effective plasmon-mediated degradation of PE MPs under visible light irradiation.

https://doi.org/10.1021/jacs.5c18907
J. Am. Chem. Soc. 2026, 148, 3462−3471

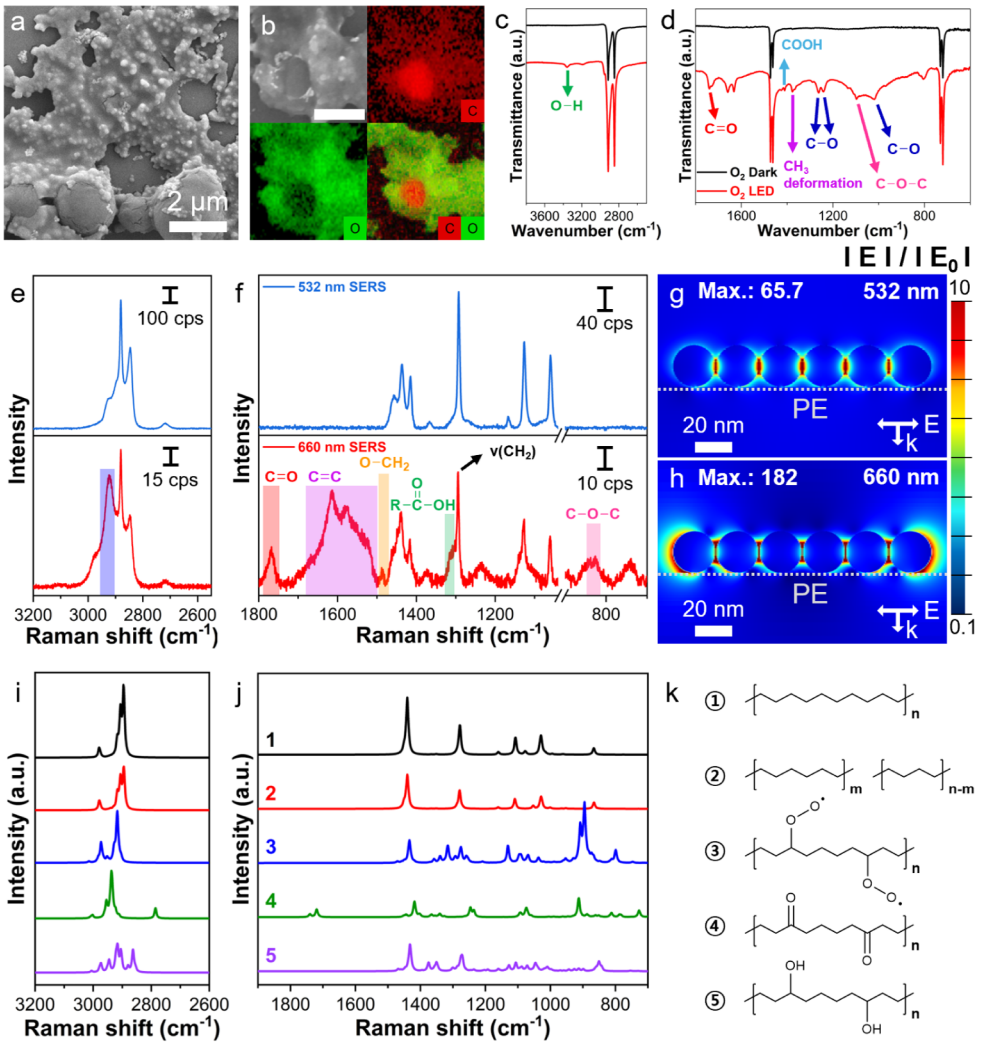

Figure 4. Characterizations of plasmon-mediated degradation of PE MPs under O_2-saturated conditions. (a) SEM image of PE MPs after 12 h of light irradiation. (b) SEM and corresponding EDS elemental mapping images of reacted PE MPs. (c, d) FTIR spectra of PE MPs before and after reaction under dark and LED irradiation, indicating the formation of oxidation species (c: 3800−2500 cm^{-1}, d: 1800−600 cm^{-1}). (e, f) SERS spectra of reacted PE MPs by using λ_{ex} of 532 (blue) and 660 nm (red). FDTD-simulated $|E|/|E_0|$ distributions of Au NPCs with a λ_{ex} (g) 532 and (h) 660 nm excitation, showing e-field enhancement around the Au NPCs. (i, j) DFT-simulated Raman spectra for degradation product models 1−5 in (k) (i: 3200−2600 cm^{-1}, j: 1900−700 cm^{-1}). (k) Molecular structures of simulated models.

Identification of Reactive Species in Plasmon-Mediated Degradation of PE MPs

To elucidate whether the degradation of PE MPs occurs via a plasmon-mediated mechanism, we tracked the degradation progress over time and assessed the role of key reactive species. SEM images of MPs collected after 3, 6, 12, and 24 h of LED illumination in the presence of Au NPCs revealed a gradual decrease in average particle size, measured as 1.99, 1.82, 1.66, and 1.53 μm, respectively, compared to the initial size of 2.5 μm (Figure 3a−d and Figure S11f). In contrast, under dark conditions, no significant changes in morphology or size were observed across the same time points (Figure S11a−e). These morphological changes were further corroborated by Raman spectroscopy at the single-particle level. At each reaction time, PE MPs treated under LED illumination consistently with Au NPCs exhibited lower Raman intensity than those under dark conditions (Figure 3e,f), indicating that significant chemical transformation occurred only in the presence of light. In contrast, Raman intensity from the MPs in the dark remained unchanged over 24 h. The extent of Raman intensity reduction under LED illumination is proportional to the reaction time. To quantitatively track this change, we selected the CH_2 twisting mode at 1294 cm^{-1}, a well-resolved and representative vibrational band for polyethylene, which allows for robust comparison with particle size change.[49] The relative intensity of this band, referenced to its initial value at 0 h, decreased to 0.68, 0.56, 0.30, and 0.28 after 3, 6, 12, and 24 h of LED illumination, respectively.

In contrast, the intensity remained nearly unchanged (~1.0) under dark conditions. These results were plotted alongside the average particle size in Figure 3g, revealing a strong correlation between the attenuation of the 1294 cm^{-1} band and the decrease in MP particle size. Notably, both parameters exhibited minimal changes after 12 h, indicating saturation in the extent of chemical degradation. Such saturation behavior is commonly observed in plasmonic catalysis when sustaining the coupled hot carrier reaction cycle becomes limited by the availability of electron acceptors and other key reactive species.[30−35] Consistent with this interpretation, PE MP size distributions collected at a fixed reaction time of 12 h showed a

https://doi.org/10.1021/jacs.5c18907
J. Am. Chem. Soc. 2026, 148, 3462−3471

clear dependence on LED power (Figure S12), with the average MP size increasing from 1.84 μm at 1.0 W to 2.04 μm at 0.5 W relative to the standard 1.7 W (410 mW/cm^2) condition. The greater size reduction at higher LED power is consistent with enhanced degradation under stronger illumination, providing additional support for a plasmon-mediated degradation pathway.

To elucidate the involvement of reactive species in the plasmon-mediated degradation process, we conducted control experiments using radical scavengers and gas-saturated environments. After 3 h of visible-light irradiation with Au NPCs, negligible changes in both morphology and Raman spectra were observed for PE MPs treated with tert-butanol (TBA), a hydroxyl radical (·OH) scavenger,[51] or under N_2-saturated conditions, compared to their respective dark controls, indicating minimal degradation (Figure 3h,i, and Figure S13). In contrast, MPs exposed to p-benzoquinone (PBQ), a scavenger of superoxide O_2- or hot electrons,[51] and those under O_2-saturated conditions showed pronounced size reductions (from 2.5 to 1.65 and 1.59 μm, respectively) and a marked attenuation of Raman intensity across the full spectral range (Figure 3h, i, and Figure S13).

To quantitatively evaluate these trends, we selected the CH_2 twisting mode at 1294 cm^{-1} as a representative vibrational feature and calculated the I_{LED}/I_{Dark} ratio for each treatment. As shown in Figure 3j, this ratio, plotted alongside the corresponding MP sizes, clearly differentiates effective degradation environments (PBQ and O_2) from suppressed ones (TBA and N_2). These results collectively implicate ·OH radicals and molecular oxygen as key reactive species in the hot carrier-induced plasmonic mechanism for PE MP degradation.

To further reconcile the complementary roles of hot electrons and hot holes in plasmon-mediated PE MP degradation, we performed additional control experiments under N_2-saturated conditions with PBQ in the dark and under LED illumination and separately carried out a hole-scavenging control in pure ethanol (EtOH) (Figure S14). The observation of clear degradation under N_2 with PBQ under illumination, relative to the corresponding dark control, indicates that the plasmon-mediated degradation can proceed even in the absence of molecular oxygen when an alternative electron acceptor is available to sustain the plasmon-driven reaction cycle. In contrast, the negligible degradation observed in pure EtOH highlights the essential contribution of hot hole-involved oxidation in the aqueous conditions, consistent with the importance of ·OH radical-related pathways in PE MP degradation. Taken together, these results support that the observed degradation is driven by plasmon-mediated activation of reactive oxygen species, rather than by thermal or photolytic effects.

Advantages of SERS in the Characterization of MPs

To further intensify the plasmon-mediated degradation reaction, we conducted the reaction under O_2-saturated conditions for 12 h to enhance oxidative pathways and produce sufficient degradation products for detailed spectroscopic analysis. SEM images showed morphological destruction of MPs to the extent that their average particle size could not be determined (Figure 4a). The surface exhibited irregular and fragmented morphologies composed of nanoscale features, suggesting that the MPs were cleaved into oxidized residues of nanometric dimensions. Elemental mapping further confirmed the oxidation of the MPs, as shown by the spatial overlap between oxygen (green) and carbon (red) signals in the EDS maps (Figure 4b). Notably, this nanoscale fragmentation is not necessarily a terminal state. Under prolonged O_2-saturated illumination for 72 h, we detected gaseous products (Figure S15), indicating that these smaller oxidized fragments can be further converted when the plasmon-driven reaction cycle is sustained.

To identify the associated chemical changes, FTIR spectra of the reacted MPs were collected after a concentration step involving solvent evaporation (see the Supporting Information for experimental details). As shown in Figure 4c,d, the FTIR spectra showed distinct features corresponding to O−H (3400 cm^{-1}), C═O (1700 cm^{-1}), symmetric COOH stretching (1410 cm^{-1}), C−O (1000−1200 cm^{-1}), and C−O−C (1050−1100 cm^{-1}) vibrations, confirming oxidative degradation through the plasmon-mediated reaction pathway.[23,52] However, as IR spectroscopy provides bulk-averaged information, it cannot selectively probe interfacial species formed at the catalyst-plastic boundary.

Given that plasmon-mediated PE degradation proceeds via heterogeneous catalysis, where chemical reactions occur at the surface, techniques capable of resolving interfacial chemistry are essential. Raman spectroscopy enables spatially localized measurements at the single-particle level, but the detected signal still originates from the entire focal volume, lacking intrinsic surface selectivity. Raman spectra at both 532 and 660 nm excitation, obtained from the reacted PE MPs, showed no distinct oxidation-related peaks relative to FTIR spectra (Figure 4c,d), showing only an overall decrease in signal intensity compared to the initial state (Figure S16).

In contrast, SERS utilizes the intense e-fields near plasmonic substrates to selectively amplify Raman signals from molecules located within the near-surface region. For SERS measurements, the reacted PE MP sample previously used for Raman analysis was subsequently coated with Au NPCs via spin coating to form the SERS platform (Figure S17). Using Au NPCs as SERS substrates, SERS spectra were obtained under both 532 and 660 nm excitation (Figure 4e,f). At 532 nm excitation, the SERS spectra showed approximately a 2-fold increase in overall intensity compared to Raman measurements (Figure S18a); however, no distinct oxidation-related peaks were observed relative to FTIR spectra (Figure 4c,d). Interestingly, switching to 660 nm excitation at the same measurement position revealed distinct oxidation-related modes relative to SERS measurements at 532 nm excitation, including C═O (1780 cm^{-1}), C═C (1600 cm^{-1}), O−CH_2 (1488 cm^{-1}), and C−O−C (850 cm^{-1}) vibrations,[51−53] with nearly 16-fold overall intensity enhancement relative to Raman at 660 nm excitation (Figure S18b).

To understand the origin of this wavelength-dependent difference in SERS response, we performed FDTD simulations of the e-field distribution for Au NPCs on PE under both excitation conditions. The simulations revealed much stronger e-field localization at the PE surface and within nanogaps for 660 nm than for 532 nm excitation (Figure 4g,h). This trend remained robust upon varying the incident angle and under unpolarized excitation, consistent with the lack of a uniform illumination orientation in experiments (Figure S19). This enhanced confinement facilitates stronger interaction with the nanoscale oxidized residues observed in SEM images (Figure 4a,b), providing a mechanistic explanation for the improved surface sensitivity and the selective detection of interfacial oxidation species.

https://doi.org/10.1021/jacs.5c18907
J. Am. Chem. Soc. 2026, 148, 3462−3471

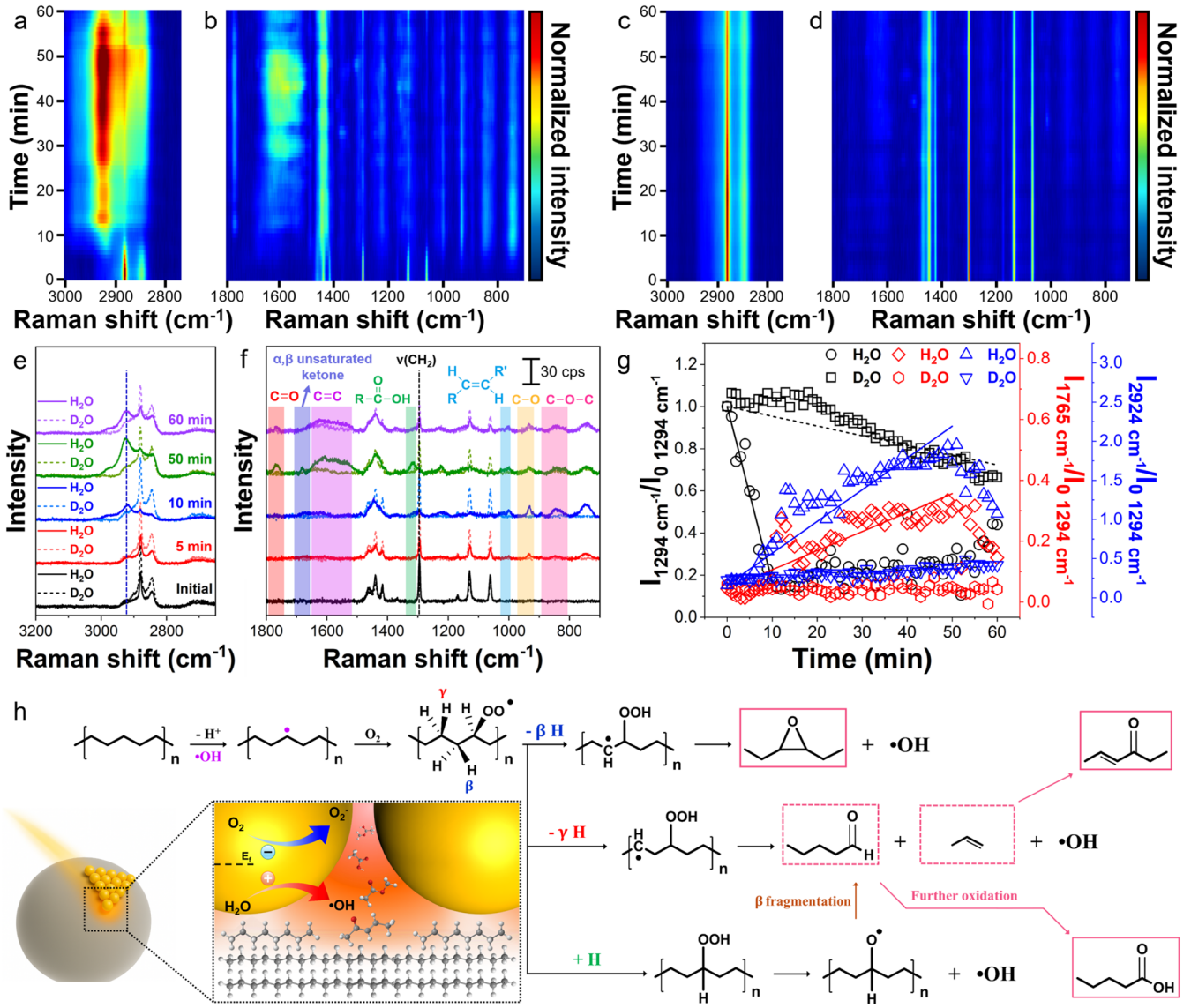

Figure 5. In situ SERS monitoring plasmon-mediated PE MP degradation. Time-resolved relative SERS intensity maps obtained during the plasmon-mediated PE MP degradation catalyzed by the Au NPCs in (a, b) H_2O and (c, d) D_2O with a λ_{ex} of 660 nm (acquisition time: 15 s). (e, f) Representative SERS spectra of PE MPs taken from panels (a–d). (g) The plots of relative SERS intensity for $\nu(CH_2$, 1294 $cm^{-1})$, $\nu(C{=}O$, 1760 $cm^{-1})$, and ν(products, 2924 cm^{-1}) in H_2O and D_2O. (h) The proposed mechanism of PE MP degradation based on in situ SERS monitoring.

To further identify these oxidation products, we calculated the vibrational modes of plausible PE degradation products using density functional theory (DFT) calculations, and the resulting spectra were compared with the experimental SERS data (Figure 4i–k). Comparison with the calculated spectra allowed assignment of the SERS band at 2924 cm^{-1}, observed under 660 nm excitation, to symmetric C–H stretching vibrations of terminal groups and related modes arising from degraded PE (Figure 4e,i, Table S1, and Figure S20). Notably, while previous studies have typically relied on the emergence of C═O bands to evaluate PE degradation, such criteria overlook the diversity of byproducts formed during the PE degradation. The 2924 cm^{-1} band may serve as an alternative indicator that more broadly reflects molecular changes associated with diverse degradation products. Additional bands corresponding to C═O, C═C, O–CH_2, and C–O–C vibrations were also matched between experimental and simulated spectra (Figure 4f,j).

From these results, we demonstrate that Au NPCs not only act as efficient plasmonic catalysts for heterogeneous degradation of PE MPs under reaction conditions but also serve as SERS substrates that enable surface-selective molecular detection under probing conditions. This dual functionality highlights the potential for in situ SERS monitoring of PE MP degradation in real time, as shown in the next section.

Real-Time Tracking of Plasmon-Mediated Degradation of PE MPs via SERS

We applied in situ SERS monitoring to directly track the plasmon-mediated degradation of PE MPs in aqueous solution under 660 nm laser irradiation. The Au NPCs act simultaneously as both Raman excitation platform and reaction-driving source. To establish a reference experiment, we first obtained time-resolved Raman intensity maps of PE MPs dispersed in aqueous solution under 660 nm excitation (Figure S21a and b). These maps were normalized to the

https://doi.org/10.1021/jacs.5c18907
J. Am. Chem. Soc. 2026, 148, 3462–3471

maximum intensity within each region, while the corresponding raw spectra are shown in Figure S21c and d. The Raman signals remained unchanged, confirming negligible degradation under these conditions. The observed peaks and their assignments are summarized in Table S2. In contrast, time-resolved SERS intensity maps obtained with the same excitation with Au NPCs (Figure 5a and b) revealed distinct spectral dynamics, with concurrent decreases and increases in specific vibrational bands. The SERS maps were likewise normalized, with the raw SERS spectra available in Figure S22. The characteristic PE vibrations at 2880 and 1294 cm^{-1}, assigned to C−H asymmetric stretching and CH_2 twisting modes, progressively decreased as the reaction proceeded, indicating the degradation of the polymer backbone. Simultaneously, new bands emerged and gradually intensified, including the 1780 and 2924 cm^{-1}, assigned to C═O stretching and degradation-related product modes, respectively. This reciprocal trend—loss of polymer-specific features alongside the rise of oxidation-associated modes—provides direct spectroscopic evidence for interfacial oxidation processes mediated by plasmonic hot carriers. Parallel experiments with D_2O under otherwise identical conditions yielded much slower spectral changes (Figure 5c and d), consistent with a kinetic isotope effect (KIE). Representative spectra extracted from these maps (Figure 5e,f) highlight this contrast, where oxygenated features such as C−O, C−O−C, C═C, and carboxyl vibrations emerged rapidly in H_2O but progressed significantly more slowly in D_2O. The reduced reactivity in D_2O indicates that ·OH radicals play a central role in the plasmon-mediated degradation process, as previously discussed.

The temporal evolution of these spectral features in H_2O further shows that early stage vibrations (C−O and C−O−C) appear within 5 min, followed by the increase of C═C and carboxyl bands at later times (Figure 5f and Table S3). In parallel, the 2924 cm^{-1} feature increases as the CH_2 twisting mode (1294 cm^{-1}) diminishes, indicating that the 2924 cm^{-1} band is a practical marker for monitoring the progression of diverse degradation pathways. Quantitative comparison of the relative SERS intensities confirms that the decay of the CH_2 twist band and the increase of oxidation-related bands are both substantially attenuated in D_2O (Figure 5g). Based on these observations, we propose a plausible mechanism for the plasmon-mediated PE degradation (Figure 5h).

CONCLUSIONS

In this study, we demonstrated Au NPCs as dual-function platforms that operate both as efficient plasmonic catalysts for the visible light-driven degradation of PE MPs and as SERS-active substrates for resolving surface-specific molecular transformations. The densely packed nanogap of Au NPCs plays a pivotal role in this dual functionality, as strong near-field localization at the interparticle junctions both amplifies hot carrier generation to drive chemical reactions and enhances SERS signals for surface-selective molecular detection. Through time-resolved experiments with reactive control species, we identified hot hole-mediated hydroxyl radicals as the dominant oxidants driving PE MP degradation. Furthermore, combined with SERS measurements under 660 nm excitation and DFT-based vibrational analysis, we identified that the 2924 cm^{-1} band can serve as a robust marker for diverse degraded products, providing a more comprehensive indicator than the conventional reliance on C═O bands alone. Time-resolved SERS monitoring revealed a sequential progression in spectral features, with early stage emergence of oxygenated vibrations accompanied by a marked increase in the 2924 cm^{-1} and concurrent attenuation of CH_2 modes. Importantly, KIE experiments performed under identical in situ SERS conditions exhibited significantly slower spectral evolution in D_2O than in H_2O, further confirming ·OH radicals as pivotal intermediates in the plasmon-mediated degradation pathway. Notably, prolonged O_2-saturated illumination produced detectable gaseous products, indicating that the oxidized fragments can undergo further conversion when plasmon-mediated degradation is sustained. Together, these results demonstrate that the Au NPCs integrate catalytic activity with spectroscopic sensitivity, enabling mechanistic insights into polymer degradation that were previously inaccessible. This plasmon-enabled strategy paves the way toward advancing the molecular-level study of persistent pollutant transformations while informing the design of plasmonic catalysts for environmental remediation and sustainable catalysis.

ASSOCIATED CONTENT

Supporting Information

The Supporting Information is available free of charge at https://pubs.acs.org/doi/10.1021/jacs.5c18907.

Experimental and theoretical methods, UV−vis spectra, simulation results, FT-IR spectra, SEM and TEM images, and tables assigning Raman and SERS peak positions (PDF)

AUTHOR INFORMATION

Corresponding Author

Seunghoon Lee − *Department of Chemistry, Dong-A University, Busan 49315, South Korea; Department of Chemical Engineering (BK21 FOUR Graduate Program), Dong-A University, Busan 49315, South Korea;* orcid.org/0000-0001-9447-4503; Email: seunghoon@dau.ac.kr

Authors

Junyeong Yang − *Department of Chemical Engineering (BK21 FOUR Graduate Program), Dong-A University, Busan 49315, South Korea*

Minchu Kang − *Department of Chemistry, Dong-A University, Busan 49315, South Korea*

Ramesh Kumar Chitumalla − *Department of Nanoenergy Engineering, Pusan National University, Busan 46241, South Korea;* orcid.org/0000-0002-9523-7056

Emiliano Cortés − *Nanoinstitute Munich, Faculty of Physics, Ludwig-Maximilians-Universität München, München 80539, Germany;* orcid.org/0000-0001-8248-4165

Joonkyung Jang − *Department of Nanoenergy Engineering, Pusan National University, Busan 46241, South Korea;* orcid.org/0000-0001-9028-0605

Complete contact information is available at: https://pubs.acs.org/10.1021/jacs.5c18907

Notes

The authors declare no competing financial interest.

https://doi.org/10.1021/jacs.5c18907
J. Am. Chem. Soc. 2026, 148, 3462−3471

■ ACKNOWLEDGMENTS

This work was supported by the National Research Foundation of Korea (NRF) grant funded by the Korean government (MSIT) (RS-2022-NR071775, RS-2023-00220748). E.C. acknowledges funding and support from the Deutsche Forschungsgemeinschaft (DFG, German Research Foundation) under Germanýs Excellence Strategy - EXC 2089/2-390776260 e-conversion cluster, the Bavarian program Solar Energies Go Hybrid (SolTech), and the Center for NanoScience (CeNS).

■ REFERENCES

(1) Geyer, R.; Jambeck, J. R.; Law, K. L. Production, Use, and Fate of All Plastics Ever Made. *Sci. Adv.* **2017**, *3* (7), No. e1700782.
(2) Garcia, J. M.; Robertson, M. L. The Future of Plastics Recycling. *Science* **2017**, *358* (6365), 870−872.
(3) Nguyen, B.; Claveau-Mallet, D.; Hernandez, L. M.; Xu, E. G.; Farner, J. M.; Tufenkji, N. Separation and Analysis of Microplastics and Nanoplastics in Complex Environmental Samples. *Acc. Chem. Res.* **2019**, *52* (4), 858−866.
(4) Thompson, R. C.; Olsen, Y.; Mitchell, R. P.; Davis, A.; Rowland, S. J.; John, A. W.; McGonigle, D.; Russell, A. E. Lost at Sea: Where Is All the Plastic? *Science* **2004**, *304* (5672), 838.
(5) Law, K. L.; Thompson, R. C. Microplastics in the Seas. *Science* **2014**, *345* (6193), 144−145.
(6) Cózar, A.; Echevarría, F.; González-Gordillo, J. I.; Irigoien, X.; Úbeda, B.; Hernández-León, S.; Palma, Á. T.; Navarro, S.; García-de-Lomas, J.; Ruiz, A.; Fernández-de-Puelles, M. L.; Duarte, C. M. Plastic Debris in the Open Ocean. *Proc. Natl. Acad. Sci. U. S. A.* **2014**, *111* (28), 10239−10244.
(7) Allen, S.; Allen, D.; Phoenix, V. R.; Le Roux, G.; Durantez Jimenez, P.; Simonneau, A.; Binet, S.; Galop, D. Atmospheric Transport and Deposition of Microplastics in a Remote Mountain Catchment. *Nat. Geosci.* **2019**, *12* (5), 339−344.
(8) Zhang, Q.; Xu, E. G.; Li, J.; Chen, Q.; Ma, L.; Zeng, E. Y.; Shi, H. A Review of Microplastics in Table Salt, Drinking Water, and Air: Direct Human Exposure. *Environ. Sci. Technol.* **2020**, *54* (7), 3740−3751.
(9) Paul-Pont, I.; Lacroix, C.; Fernandez, C. G.; Hegaret, H.; Lambert, C.; Le Goic, N.; Frere, L.; Cassone, A.-L.; Sussarellu, R.; Fabioux, C.; et al. Exposure of Marine Mussels Mytilus spp. to Polystyrene Microplastics: Toxicity and Influence on Fluoranthene Bioaccumulation. *Environ. Pollut.* **2016**, *216*, 724−737.
(10) Hernandez, L. M.; Xu, E. G.; Larsson, H. C. E.; Tahara, R.; Maisuria, V. B.; Tufenkji, N. Plastic Teabags Release Billions of Microparticles and Nanoparticles into Tea. *Environ. Sci. Technol.* **2019**, *53* (21), 12300−12310.
(11) Zhang, F.; Zeng, M.; Yappert, R. D.; Sun, J.; Lee, Y.-H.; La Pointe, A. M.; Peters, B.; Abu-Omar, M. M.; Scott, S. L. Polyethylene Upcycling to Long-Chain Alkylaromatics by Tandem Hydrogenolysis/Aromatization. *Science* **2020**, *370* (6515), 437−441.
(12) Lopez, G.; Artetxe, M.; Amutio, M.; Bilbao, J.; Olazar, M. Thermochemical Routes for the Valorization of Waste Polyolefinic Plastics to Produce Fuels and Chemicals: A Review. *Renew. Sustain. Energy Rev.* **2017**, *73*, 346−368.
(13) Zhang, S.; Hu, Q.; Zhang, Y.-X.; Guo, H.; Wu, Y.; Sun, M.; Zhu, X.; Zhang, J.; Gong, S.; Liu, P.; Niu, Z. Depolymerization of Polyesters by a Binuclear Catalyst for Plastic Recycling. *Nat. Sustain.* **2023**, *6* (8), 965−973.
(14) Zeng, W.; Zhao, Y.; Zhang, F.; Li, R.; Tang, M.; Chang, X.; Wang, Y.; Wu, F.; Han, B.; Liu, Z. A General Strategy for Recycling Polyester Wastes into Carboxylic Acids and Hydrocarbons. *Nat. Commun.* **2024**, *15* (1), 160.
(15) Gao, R.; Liu, R.; Sun, C. A Marine Fungus Alternaria alternata FB1 Efficiently Degrades Polyethylene. *J. Hazard. Mater.* **2022**, *431*, 128617.
(16) Hu, X.; Gu, H.; Wang, Y.; Liu, J.; Yu, Z.; Li, Y.; Jin, J.; Liu, X.; Dai, Q.; Wang, G. Succession of Soil Bacterial Communities and Network Patterns in Response to Conventional and Biodegradable Microplastics: A Microcosmic Study in Mollisol. *J. Hazard. Mater.* **2022**, *436*, 129218.
(17) Zhang, S.; Xia, B.; Qu, Y.; Jing, L.; Jaroniec, M.; Ran, J.; Qiao, S.-Z. Photocatalytic Production of Ethylene and Propionic Acid from Plastic Waste by Titania-Supported Atomically Dispersed Pd Species. *Sci. Adv.* **2023**, *9* (49), No. eadk2407.
(18) Wang, L.; Jiang, S.; Gui, W.; Li, H.; Wu, J.; Wang, H.; Yang, J. Photocatalytic Upcycling of Plastic Waste: Mechanism, Integrating Modus, and Selectivity. *Small Struct.* **2023**, *4* (10), 2300142.
(19) Ali, S. S.; Qazi, I. A.; Arshad, M.; Khan, Z.; Voice, T. C.; Mehmood, C. T. Photocatalytic Degradation of Low Density Polyethylene (LDPE) Films Using Titania Nanotubes. *Environ. Nanotechnol. Monit. Manage.* **2016**, *5*, 44−53.
(20) Nabi, I.; Bacha, A.-U.-R.; Li, K.; Cheng, H.; Wang, T.; Liu, Y.; Ajmal, S.; Yang, Y.; Feng, Y.; Zhang, L. Complete Photocatalytic Mineralization of Microplastic on TiO_2 Nanoparticle Film. *iScience* **2020**, *23* (7), 101326.
(21) Uheida, A.; Giraldo Mejía, H.; Abdel-Rehim, M.; Hamd, W.; Dutta, J. Visible Light Photocatalytic Degradation of Polypropylene Microplastics in a Continuous Water Flow System. *J. Hazard. Mater.* **2021**, *406*, 124299.
(22) Bertoldo, M.; Bronco, S.; Cappelli, C.; Gragnoli, T.; Andreotti, L. Combining Theory and Experiment to Study the Photooxidation of Polyethylene and Polypropylene. *J. Phys. Chem. B* **2003**, *107* (43), 11880−11888.
(23) Jiao, X.; Zheng, K.; Chen, Q.; Li, X.; Li, Y.; Shao, W.; Xu, J.; Zhu, J.; Pan, Y.; Sun, Y.; et al. Photocatalytic Conversion of Waste Plastics into C_2 Fuels under Simulated Natural Environment Conditions. *Angew. Chem., Int. Ed.* **2020**, *59* (36), 15497−15501.
(24) Miao, Y.; Zhao, Y.; Gao, J.; Wang, J.; Zhang, T. Direct Photoreforming of Real-World Polylactic Acid Plastics into Highly Selective Value-Added Pyruvic Acid under Visible Light. *J. Am. Chem. Soc.* **2024**, *146* (7), 4842−4850.
(25) Uekert, T.; Kasap, H.; Reisner, E. Photoreforming of Nonrecyclable Plastic Waste over a Carbon Nitride/Nickel Phosphide Catalyst. *J. Am. Chem. Soc.* **2019**, *141* (38), 15201−15210.
(26) Zhang, S.; Johannessen, B.; Xia, B.; Gao, X.; Davey, K.; Ran, J.; Qiao, S.-Z. Selective Oxidation of Polyesters via PdCu−TiO_2 Photocatalysts in Flow. *J. Am. Chem. Soc.* **2024**, *146* (46), 32003−32012.
(27) Huang, Z.; Shanmugam, M.; Liu, Z.; Brookfield, A.; Bennett, E. L.; Guan, R.; Vega Herrera, D. E.; Lopez-Sanchez, J. A.; Slater, A. G.; McInnes, E. J. L.; Qi, X.; Xiao, J. Chemical Recycling of Polystyrene to Valuable Chemicals via Selective Acid-Catalyzed Aerobic Oxidation under Visible Light. *J. Am. Chem. Soc.* **2022**, *144* (14), 6532−6542.
(28) Lin, J.; Hu, K.; Wang, Y.; Tian, W.; Hall, T.; Duan, X.; Sun, H.; Zhang, H.; Cortés, E.; Wang, S. Tandem Microplastic Degradation and Hydrogen Production by Hierarchical Carbon Nitride−Supported Single-Atom Iron Catalysts. *Nat. Commun.* **2024**, *15*, 8769.
(29) Lin, L.; Yi, J.; Wang, J.; Qian, Q.; Chen, Q.; Cao, C.; Zhou, W. Enhancing Microplastic Degradation through Synergistic Photocatalytic and Pretreatment Approaches. *Langmuir* **2024**, *40* (43), 22582−22590.
(30) Cortés, E. Activating Plasmonic Chemistry: Plasmonic Photocatalysts Can Reduce Activation Barriers and Unlock Reaction Pathways. *Science* **2018**, *362* (6410), 28−29.
(31) Zhang, Y.; He, S.; Guo, W.; Hu, Y.; Huang, J.; Mulcahy, J. R.; Wei, W. D. Surface-Plasmon-Driven Hot Electron Photochemistry. *Chem. Rev.* **2018**, *118* (6), 2927−2954.
(32) Zhou, L.; Swearer, D. F.; Zhang, C.; Robatjazi, H.; Zhao, H.; Henderson, L.; Dong, L.; Christopher, P.; Carter, E. A.; Nordlander, P.; et al. Quantifying Hot Carrier and Thermal Contributions in Plasmonic Photocatalysis. *Science* **2018**, *362* (6410), 69−72.
(33) Peiris, E.; Hanauer, S.; Le, T.; Wang, J.; Salavati-Fard, T.; Brasseur, P.; Formo, E. V.; Wang, B.; Camargo, P. H. C. Controlling Selectivity in Plasmonic Catalysis: Switching Reaction Pathway from

https://doi.org/10.1021/jacs.5c18907
J. Am. Chem. Soc. 2026, 148, 3462−3471

Hydrogenation to Homocoupling Under Visible-Light Irradiation. *Angew. Chem., Int. Ed.* **2023**, *62* (4), No. e202216398.
(34) Yuan, Y.; Zhou, L.; Robatjazi, H.; Bao, J. L.; Zhou, J.; Bayles, A.; Yuan, L.; Lou, M.; Lou, M.; Khatiwada, S.; et al. Earth-Abundant Photocatalyst for H_2 Generation from NH_3 with Light-Emitting Diode Illumination. *Science* **2022**, *378* (6622), 889−893.
(35) Aslam, U.; Rao, V. G.; Chavez, S.; Linic, S. Catalytic Conversion of Solar to Chemical Energy on Plasmonic Metal Nanostructures. *Nat. Catal.* **2018**, *1*, 656−665.
(36) Kang, Y.; João, S. M.; Lin, R.; Liu, K.; Zhu, L.; Fu, J.; Cheong, W.-C.; Lee, S.; Frank, K.; Nickel, B.; et al. Effect of Crystal Facets in Plasmonic Catalysis. *Nat. Commun.* **2024**, *15*, 3923.
(37) Herran, M.; Juergensen, S.; Kessens, M.; Hoeing, D.; Köppen, A.; Sousa-Castillo, A.; Parak, W. J.; Lange, H.; Reich, S.; Schulz, F.; Cortés, E. Plasmonic Bimetallic Two-Dimensional Supercrystals for H_2 Generation. *Nat. Catal.* **2023**, *6*, 1205−1214.
(38) Lee, S.; Hwang, H.; Lee, W.; Schebarchov, D.; Wy, Y.; Grand, J.; Auguié, B.; Wi, D. H.; Cortés, E.; Han, S. W. Core−Shell Bimetallic Nanoparticle Trimers for Efficient Light-to-Chemical Energy Conversion. *ACS Energy Lett.* **2020**, *5* (12), 3881−3890.
(39) Gargiulo, J.; Berté, R.; Li, Y.; Maier, S. A.; Cortés, E. From Optical to Chemical Hot Spots in Plasmonics. *Acc. Chem. Res.* **2019**, *52* (9), 2525−2535.
(40) Lee, S.; Kim, J.; Yang, H.; Cortés, E.; Kang, S.; Han, S. W. Particle-in-a-Frame Nanostructures with Interior Nanogaps. *Angew. Chem., Int. Ed* **2019**, *58* (44), 15890−15894.
(41) Lee, S.; Wy, Y.; Lee, Y.; Ham, K.; Han, S. W. Core−Shell Nanoparticle Clusters Enable Synergistic Integration of Plasmonic and Catalytic Functions in a Single Platform. *Small* **2017**, *13* (43), 1701633.
(42) Yoon, S. Controlled assembly of gold nanoparticles: Methods and plasmon coupling properties. *Bull. Korean Chem. Soc.* **2024**, *45* (8), 689−698.
(43) Sobhani, Z.; Zhang, X.; Gibson, C.; Naidu, R.; Megharaj, M.; Fang, C. Identification and Visualisation of Microplastics/Nanoplastics by Raman Imaging (i): Down to 100 nm. *Water Res.* **2020**, *174*, 115658.
(44) Xie, L.; Gong, K.; Liu, Y.; Zhang, L. Strategies and Challenges of Identifying Nanoplastics in Environment by Surface-Enhanced Raman Spectroscopy. *Environ. Sci. Technol.* **2023**, *57* (1), 25−43.
(45) Lee, S.; Kang, S.; Kim, J.; Wy, Y.; Han, S. W. Colloidal Clusters of Plasmonic Nanoparticles with Controlled Topological Parameters. *ChemNanomater* **2017**, *3* (10), 772−778.
(46) Stefancu, A.; Aizpurua, J.; Alessandri, I.; Bald, I.; Baumberg, J. J.; Besteiro, L.; Christopher, P.; Correa-Duarte, M.; de Nijs, B.; Demetriadou, A.; Frontiera, R. R.; Fukushima, T.; Halas, N. J.; Jain, P. K.; Kim, Z. H.; Kurouski, D.; Lange, H.; Li, J.-F.; Liz-Marzán, L. M.; Lucas, I. T.; Meixner, A. J.; Murakoshi, K.; Nordlander, P.; Peveler, W. J.; Quesada-Cabrera, R.; Ringe, E.; Schatz, G. C.; Schlücker, S.; Schultz, Z. D.; Tan, E. X.; Tian, Z.-Q.; Wang, L.; Weckhuysen, B. M.; Xie, W.; Ling, X.; Zhang, J.; Zhao, Z.; Zhou, R.-Y.; Cortés, E. Impact of Surface-Enhanced Raman Spectroscopy in Catalysis. *ACS Nano* **2024**, *18* (43), 29337−29379.
(47) Zhang, M. D.; Wang, T.; Du, X. M.; Mao, Y.; Zhu, A. N.; Du, A. X.; Tong, L. B.; Xie, W. Observation of N_2H_3 Intermediates by *In Situ* Electrochemical SERS: New Pathway of Ammonia Oxidation on High-Durability PtIr Catalysts. *J. Am. Chem. Soc.* **2025**, *147* (31), 28331−28339.
(48) Du, X. M.; Du, A. X.; Wang, D.; Mao, Y.; Zhang, Z.; Xie, W. Surface-Enhanced Raman Spectroscopic Study of Key Intermediates in Electrochemical Ammonia Decomposition. *J. Am. Chem. Soc.* **2025**, *147* (10), 8083−8087.
(49) Yi, J.; You, E.-M.; Hu, R.; Wu, D.-Y.; Liu, G.-K.; Yang, Z.-L.; Zhang, H.; Gu, Y.; Wang, Y.-H.; Wang, X.; et al. Surface-enhanced Raman spectroscopy: A half-century historical perspective. *Chem. Soc. Rev.* **2025**, *54* (3), 1453−1551.
(50) Wei, Y.; Fan, X.; Chen, D.; Zhu, X.; Yao, L.; Zhao, X.; Tang, X.; Wang, J.; Zhang, Y.; Qiu, T.; Hao, Q. Probing Oxidation Mechanisms in Plasmonic Catalysis: Unraveling the Role of Reactive Oxygen Species. *Nano Lett.* **2024**, *24* (6), 2110−2117.
(51) Mayorga, C.; Athalye, S. M.; Boodaghidizaji, M.; Sarathy, N.; Hosseini, M.; Ardekani, A.; Verma, M. S. Limit of Detection of Raman Spectroscopy Using Polystyrene Particles from 25 to 1000 nm in Aqueous Suspensions. *Anal. Chem.* **2025**, *97* (16), 8908−8914.
(52) Phan, S.; Padilla-Gamiño, J. L.; Luscombe, C. K. The Effect of Weathering Environments on Microplastic Chemical Identification with Raman and IR Spectroscopy: Part I. Polyethylene and Polypropylene. *Polym. Test* **2022**, *116*, 107752.
(53) Santos, M. J. L.; Brolo, A. G.; Girotto, E. M. Study of Polaron and Bipolaron States in Polypyrrole by *In Situ* Raman Spectroelectrochemistry. *Electrochim. Acta* **2007**, *52* (20), 6141−6145.

https://doi.org/10.1021/jacs.5c18907
J. Am. Chem. Soc. 2026, 148, 3462−3471